

## Assembly of Modular Asymmetric Organic-Inorganic Polyoxometalate Hybrids into Anisotropic Nanostructures

Mali H. Rosnes<sup>1</sup>, Chiara Musumeci<sup>2</sup>, Chullikkattil P. Pradeep<sup>1</sup>, Jennifer S. Mathieson<sup>1</sup>, De-Liang Long<sup>1</sup>, Yufei Song<sup>1</sup>, Bruno Pignataro<sup>3\*</sup>, Richard Cogdell<sup>4\*</sup> and Leroy Cronin<sup>1\*</sup>

<sup>1</sup>WestCHEM, School of Chemistry, University of Glasgow, Joseph Black Building, University Avenue, Glasgow, UK G12 8QQ, <sup>2</sup>Superlab - Consorzio Catania Ricerche, S.le Primosole 50, 95121 Catania, Italy, <sup>3</sup>Dipartimento di Chimica Fisica "F. Accascina", Università di Palermo, V.le delle Scienze, Parco D'Orleans II; Ed.17 - 90128 Palermo, Italy, <sup>4</sup>Glasgow Biomedical Research Centre, University of Glasgow, University Avenue, Glasgow, G12 8QQ, UK.

RECEIVED DATE (automatically inserted by publisher); E-mail:

[L.Cronin@chem.gla.ac.uk](mailto:L.Cronin@chem.gla.ac.uk); [r.cogdell@bio.gla.ac.uk](mailto:r.cogdell@bio.gla.ac.uk); [bruno.pignataro@unipa.it](mailto:bruno.pignataro@unipa.it)

### Table of Contents:

1. General Materials and Methods.....	S2
2. Experimental Procedure.....	S4
1. <i>Synthesis and Characterisation of Compound 1</i> .....	S4
2. <i>Synthesis and Characterisation of Compound 2</i> .....	S8
3. <i>Synthesis and Characterisation of Compound 3</i> .....	S14
3. Mass Spectra Discussion.....	S15
4. UV Discussion.....	S16
5. Self-assembly on surfaces.....	S17
6. X-ray Crystallography.....	S26
1. <i>Crystallographic studies of Compound 1</i> .....	S26
2. <i>Crystallographic studies of Compound 2</i> .....	S26
7. References.....	S26

## 1. General Materials and Methods:

(TBA)<sub>4</sub>[ $\alpha$ -Mo<sub>8</sub>O<sub>26</sub>] (where TBA = tertbutylammonium bromide),<sup>1</sup> TRIS derivatized pyrene (which = H<sub>3</sub>L<sup>1</sup> ((HOCH<sub>2</sub>)<sub>3</sub>CNH-CH<sub>2</sub>-C<sub>16</sub>H<sub>9</sub>)<sup>2</sup> and C<sub>9</sub>-terminal alkene (which = H<sub>3</sub>L<sup>2</sup> ((HOCH<sub>2</sub>)<sub>3</sub>C-C<sub>9</sub>H<sub>17</sub>)<sup>3</sup> were all synthesized from literature procedures. All other materials were purchased from Sigma Aldrich Chemicals and used without further purification.

**Electrospray Mass Spectroscopic Measurements:** All MS data were collected using a Q-trap, time-of-flight MS (MicrOTOF-Q MS) instrument equipped with an electrospray (ESI) source supplied by Bruker Daltonics Ltd. All analyses were carried out at 180°C in acetonitrile, collected in negative ion mode and the spectrometer was calibrated with the standard tune-mix to give a precision of ca. 1.5 ppm in the region of 500-3000 *m/z*.

**Bruker Advanced 400 MHz:** <sup>1</sup>H NMR at 400 MHz with deuterated acetonitrile from Goss Scientific.

**UV-Vis Spectroscopy:** UV-Vis spectra were all collected on JASCO V-670 Spectrophotometer.

**Fourier-transform Infrared (FT-IR) Spectroscopy:** All spectra were recorded on Shimadzu FTIR 8400S Fourier Transformer Infrared Spectrophotometer. Wavenumbers ( $\tilde{\nu}$ ) are given in cm<sup>-1</sup>; intensities as denoted as wk = weak, sh = sharp, m = medium, br = broad, s = strong.

**Elemental Analysis:** Carbon, nitrogen and hydrogen content were determined by the microanalysis services within the Department of Chemistry, University of Glasgow using an EA 1110 CHNS, CE-440 Elemental Analyser.

**Single Crystal X-Ray Diffraction:** X-ray diffraction intensity data sets and unit cell verifications were collected using an Oxford Diffraction Gemini Ultra with an ATLAS

charge-coupled device (CCD) detector [ $\lambda$  ( $\text{Cu}_{K\alpha}$ ) = 1.54184 Å] at 150(2) K. Data reduction was performed using the CrysAlis software package and structure solution, and refinement was carried out using SHELXS-97<sup>9</sup> and SHELXL-97<sup>9</sup> using WinGX<sup>10</sup>. Corrections for incident and diffracted beam absorption effects were applied using analytical numeric absorption correction using a multifaceted crystal model.<sup>11</sup>

**Thermogravimetric Analysis (TGA):** Thermogravimetric analysis was performed on a TA Instruments Q 500 Thermogravimetric Analyzer under nitrogen flow at a typical heating rate of 10 °C min<sup>-1</sup>.

**Differential Scanning Calorimetric Analysis (DSC):** DSC analysis was performed on a TA instruments Q 200 calorimeter under nitrogen flow at a typical heating rate of 10 °C min<sup>-1</sup>.

**Powder X-Ray Diffraction (XRD):** Powder XRD patterns were collected on a PANalytical X'PERT Pro diffractometer ( $\lambda$  ( $\text{Cu}_{K\alpha}$ ) = 1.5405 Å) equipped with a graphite monochromator and an X'Celerator detector, in flat plate mode.

**Dynamic Scanning Force Microscopy (SFM)** was carried out in air using a Multimode Nanoscope IIIa, Digital Instruments, equipped with a phase extender apparatus and a Q-box module.<sup>4</sup> Etched-silicon probes (pyramidal-shape tip, nominal curvature 10 nm, nominal internal angle 35°) were used. During the scanning, the 125- $\mu\text{m}$ -long cantilever, with a nominal spring constant in the range of 20–100 N/m, oscillated at its resonance frequency (~330 kHz). Height and phase images were collected by capturing 512 x 512 points in each scan and the scan rate was maintained below 1 line per second. During the imaging, temperature and humidity were about 25 °C and 40 %, respectively.

**Langmuir-Blodgett Deposition** was performed through a KSV minitrough apparatus. Ultrapure Millipore water with resistivity greater than 18.2 M $\Omega$ ·cm was used as subphase. The experiments were performed at a subphase temperature of 25 °C.

## 2. Experimental Procedure:

### 1. Full synthetic procedure for Compound 1:

A mixture of (TBA)<sub>4</sub>[ $\alpha$ -Mo<sub>8</sub>O<sub>26</sub>] (1.618 g, 0.75 mmol), Mn(OAc)<sub>3</sub>·2H<sub>2</sub>O (0.305 g, 1.14 mmol), H<sub>3</sub>L<sup>1</sup> (0.437 g, 1.3 mmol) and H<sub>3</sub>L<sup>2</sup> (0.300 g, 1.3 mmol) in 45 mL of dried acetonitrile was prepared, and refluxed at 80 °C for 16 hours. The orange/brown reaction mixture was then cooled down to room temperature and the precipitate was removed by centrifugation. The volume of the solvent was reduced to half under vacuum on a rotory evaporator, and then replaced with ca. 20 ml toluene. The solution was left for slow evaporation, and batches were collected regularly as the materials precipitated out. The precipitates were then recrystallized by dissolving them in dimethylformamide and diffusing in diethyl ether in order to yield single crystals.

**Yield:** 307 mg (0.14 mmol, 14.0 % based on Mo).

**EA:** (TBA)<sub>3</sub>[MnMo<sub>6</sub>O<sub>18</sub>((OCH<sub>2</sub>)<sub>3</sub>C-C<sub>9</sub>H<sub>17</sub>)<sub>1</sub>((OCH<sub>2</sub>)<sub>3</sub>CNH-CH<sub>2</sub>-C<sub>16</sub>H<sub>9</sub>)<sub>1</sub>] (2205.65 g/mol), % found (calculated values in brackets): C 44.54 (44.65), H 6.89 (6.81), N 2.65 (2.54).

**Characteristic IR-bands:** 2959.38 (m), 2931.42 (m), 2904.41(m), 1640.00 (w), 1616.88 (w), 1570.10 (w), 1479.45 (m), 1455.85 (m), 1380.60 (w), 1110.55 (w), 1072.46 (m), 1034.36 (m), 936.47 (s), 916.22 (s), 899.82 (s), 858.83 (w), 835.69 (s), 655.34 (vs).

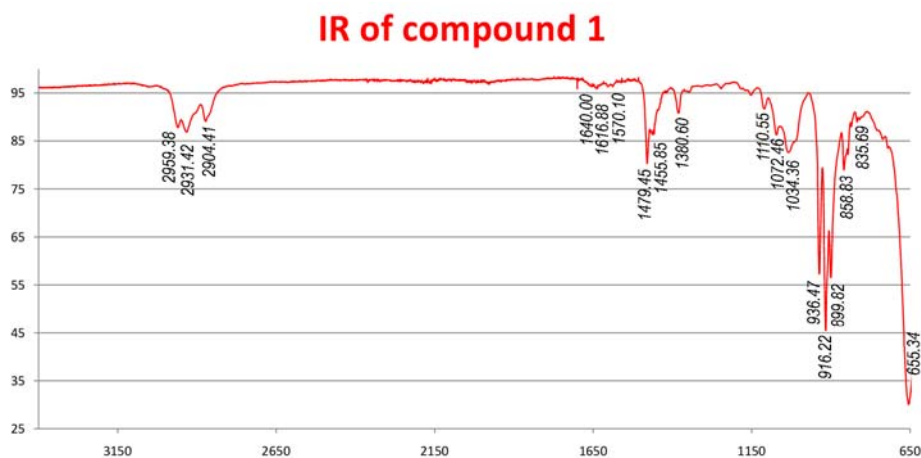


Figure S1: IR spectra of compound 1.

**$^1\text{H}$  NMR ( $\text{CD}_3\text{CN}$ , 400 MHz):**  $\delta$  0.95 (t, 36H),  $\delta$  1.34 (m, 34H),  $\delta$  1.58 (m, 24H),  $\delta$  2.04 (m, 2H),  $\delta$  3.07 (m, 24H),  $\delta$  3.99 (s, broad, 2H),  $\delta$  4.96 (dd, 2H),  $\delta$  5.84 (m, 1H),  $\delta$  7.77-8.58 (m, 12H), 61.00 (broad,  $-\text{CH}_2-$ ) ppm. The assignments of the different peaks are shown in figure S2.

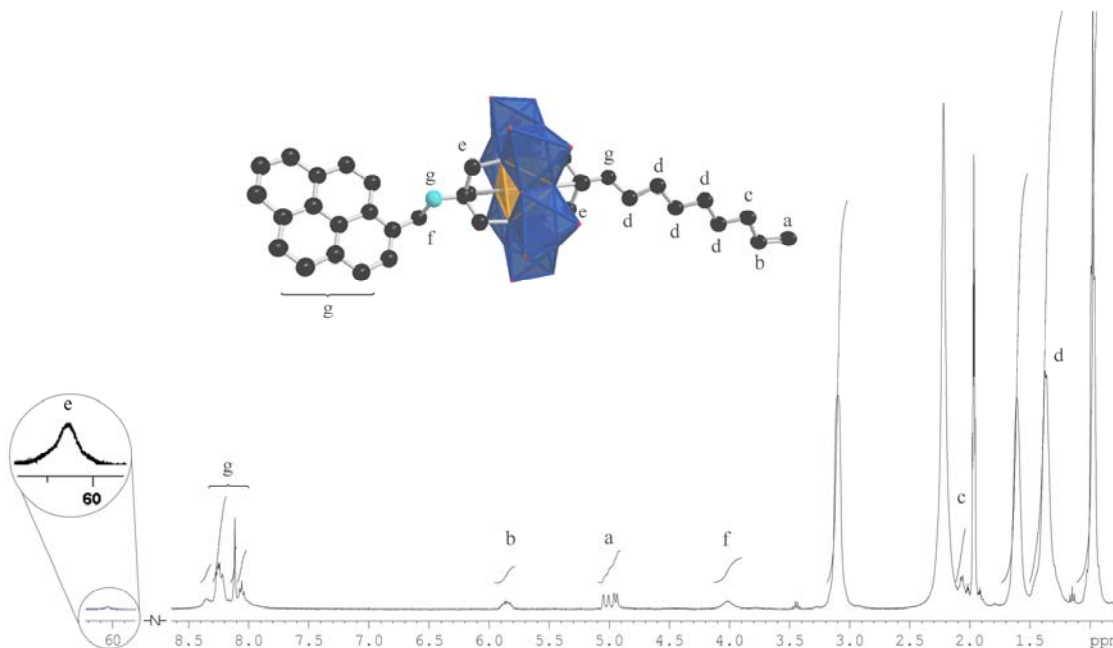


Figure S2: NMR spectra of compound **1**, with the protons from the compound labeled.

**ESI-MS:** The ESI-MS spectrum of compound **1** shows only one signal at  $m/z = 1963.15$  above 1500  $m/z$ , which can be assigned as  $(\text{TBA})_2[\text{MnMo}_6\text{O}_{18}((\text{OCH}_2)_3\text{C}-\text{C}_9\text{H}_{17})_1((\text{OCH}_2)_3\text{CNH}-\text{CH}_2-\text{C}_{16}\text{H}_9)_1]^{1-}$ .

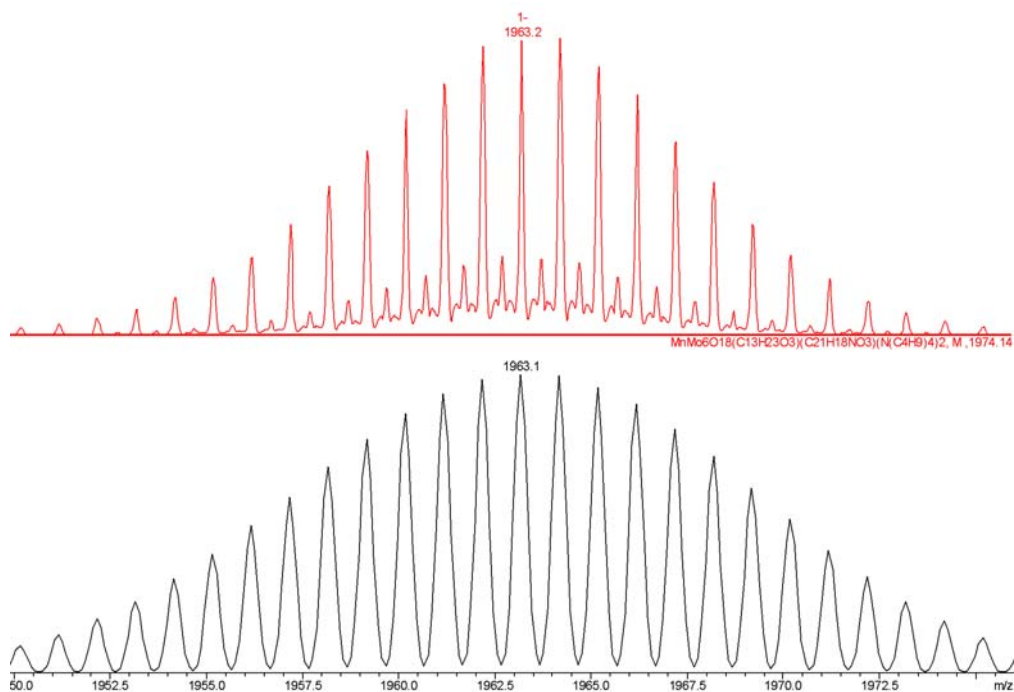


Figure S3: ESI-MS spectra of compound **1** shown in red, with the simulated MS pattern underneath for comparison.

### Thermogravimetric Analysis:

TGA shows that the cluster is stable up to 255 °C, whereupon it begins to lose its organic cations and ligand, and the cluster decomposes. The loss of 49 % corresponds to the loss of all organic material from the cluster, including the TBA counter ions.

### Thermogravimetric Analysis of Compound **1**

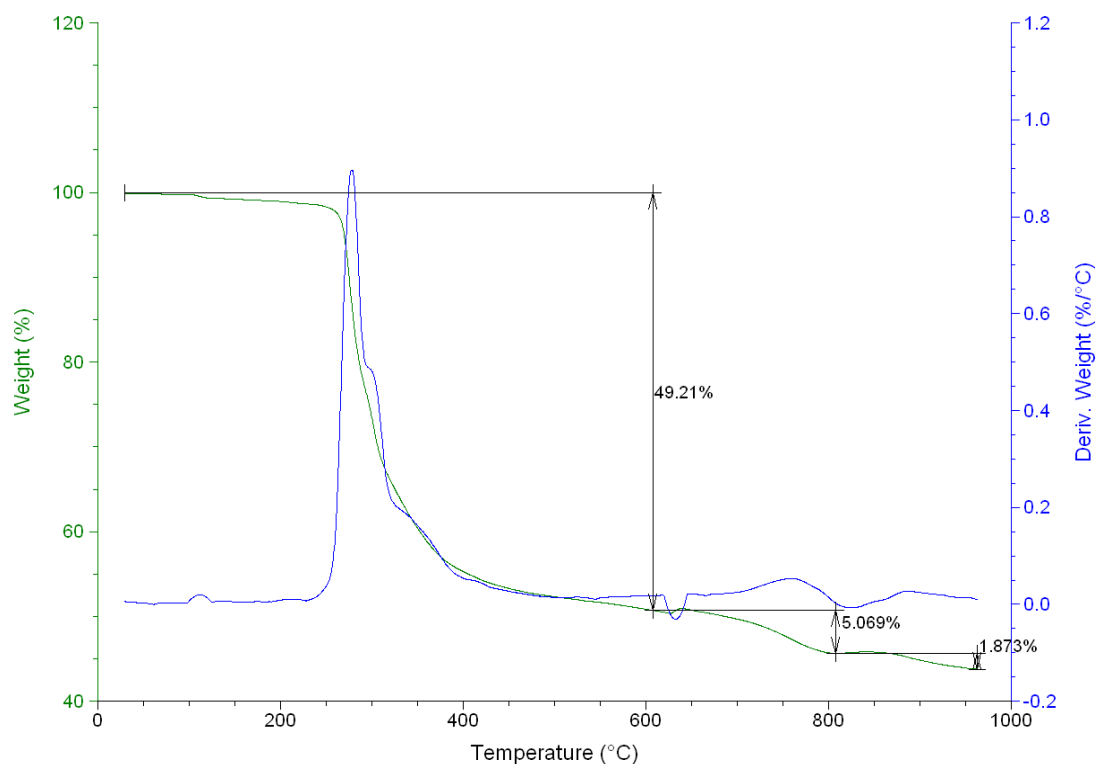
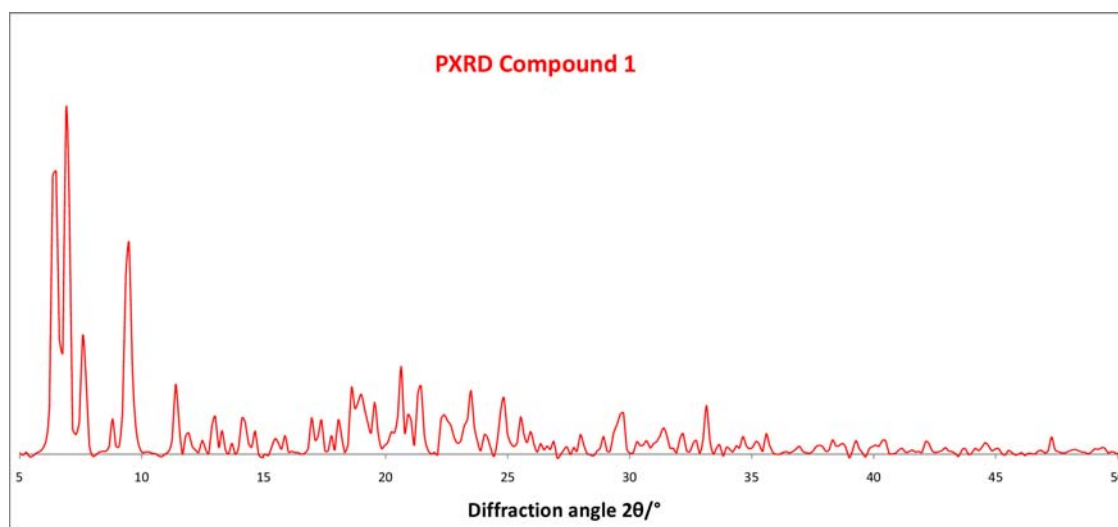


Figure S4: TGA analysis of compound **1**.

### Powder XRD analysis:

The Powder XRD pattern of the precipitate of compound **1** was collected, shown in red, and compared to the simulated PXRD pattern from the single crystal X-ray, shown in black underneath, see figure S5. The two patterns are very similar, and neither display diffraction above  $50^\circ 2\theta$ .



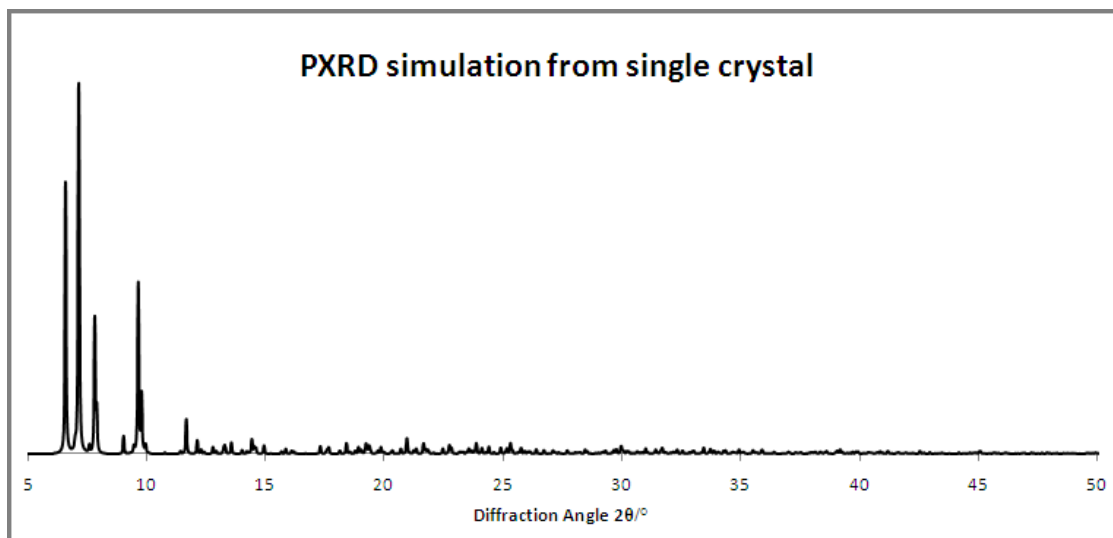


Figure S5: Powder x-ray of compound **1** (in red), with the simulated powder x-ray pattern from the single crystal shown (in black) underneath.

## 2. Full synthetic procedure for Compound **2** :

From the same reaction pot as we synthesised compound **1**, we can also observe compound **2** from the fractional crystallisation by ESI-mass spectrometry. In order to synthesize sufficient material for full characterization and further studies, the following general synthesis was applied:

A mixture of (TBA)<sub>4</sub>[ $\alpha$ -Mo<sub>8</sub>O<sub>26</sub>] (8.0 g, 3.7 mmol), Mn(OAc)<sub>3</sub>·2H<sub>2</sub>O (1.49 g, 5.6 mmol) and H<sub>3</sub>L<sup>2</sup> (2.95 g, 12.8 mmol) in 220 mL of acetonitrile was prepared, and refluxed at 80 °C for 16 hours. The orange reaction mixture was then cooled down to temperature and the precipitate was removed by centrifugation. The volume of the filtrate was reduced to half under vacuum on a rotory evaporator. The precipitate was recrystallized and single crystals were isolated using the method described for compound (**1**) (above). After ~3 days orange diamond shaped crystals were formed.

**Yield:** 7.806 g (3.7 mmol, 75.33 % based on Mo).



**EA:** (TBA)<sub>3</sub>[MnMo<sub>6</sub>O<sub>18</sub>((OCH<sub>2</sub>)<sub>3</sub>C-C<sub>9</sub>H<sub>17</sub>)<sub>2</sub>] (2100.6 g/mol) % found (calculated values in brackets): C 42.29 (42.31), H 7.47 (7.39), N 2.13 (2.00).

**Characteristic IR-bands:** 2958.9 (m), 2929.97 (m), 2872.10 (m), 1481.38 (m), 1462.09 (w), 1381.08 (w), 1236.41 (m), 1111.03 (m), 1051.24 (w), 1014.59 (m), 935.51 (s), 914.29 (s), 898.86 (s) cm<sup>-1</sup>.

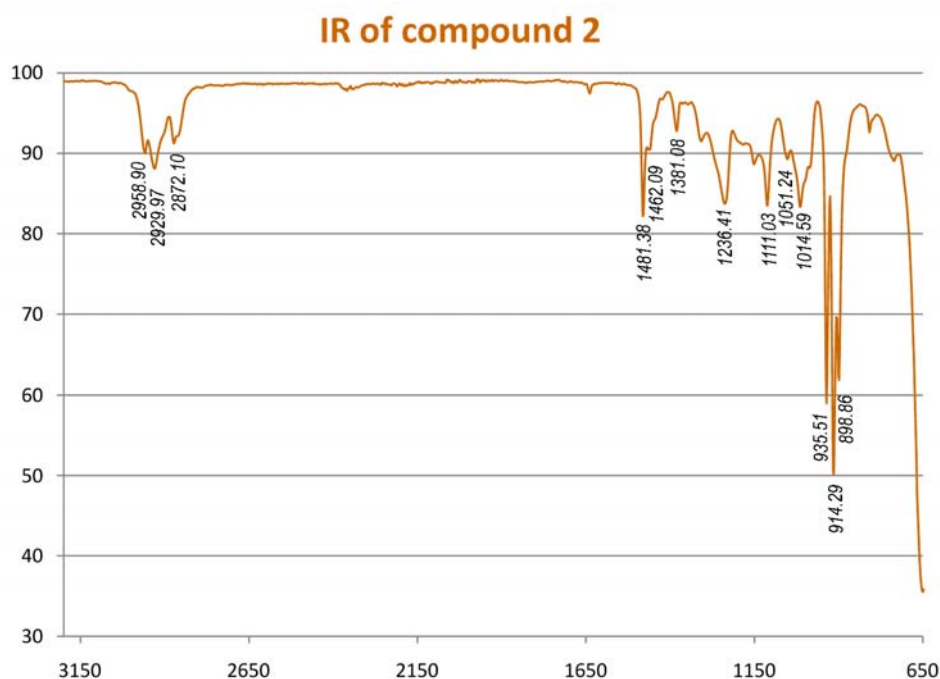


Figure S6: IR spectra of compound **2**.

**<sup>1</sup>H NMR (CD<sub>3</sub>CN, 400 MHz):** δ 0.97 (t, 36H), δ 1.18-1.74 (m, 44H), δ 1.61 (m, 24H), δ 2.03 (q, 4H), δ 3.10 (m, 24H), δ 4.95 (dd, 4H), δ 5.82 (m, 2H), δ 8.09 (s, broad, 4H), δ 60.0 (s, broad).

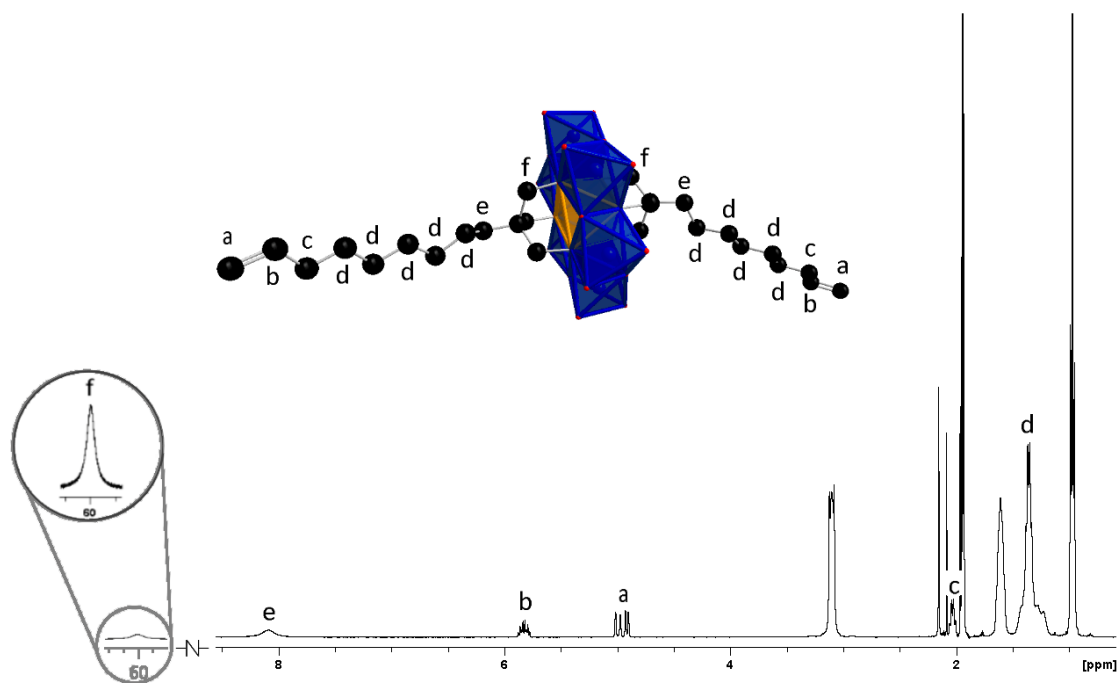


Figure S7: NMR spectra of compound **2**, with the protons from the compound labeled.

**ESI-MS:** The ESI-MS spectrum of compound **1** show one main signal at  $m/z = 1858.2$ , which can be assigned as  $(\text{TBA})_2[\text{MnMo}_6\text{O}_{18}((\text{OCH}_2)_3\text{C}-\text{C}_9\text{H}_{17})_2]^{1-}$  with no other major peaks.

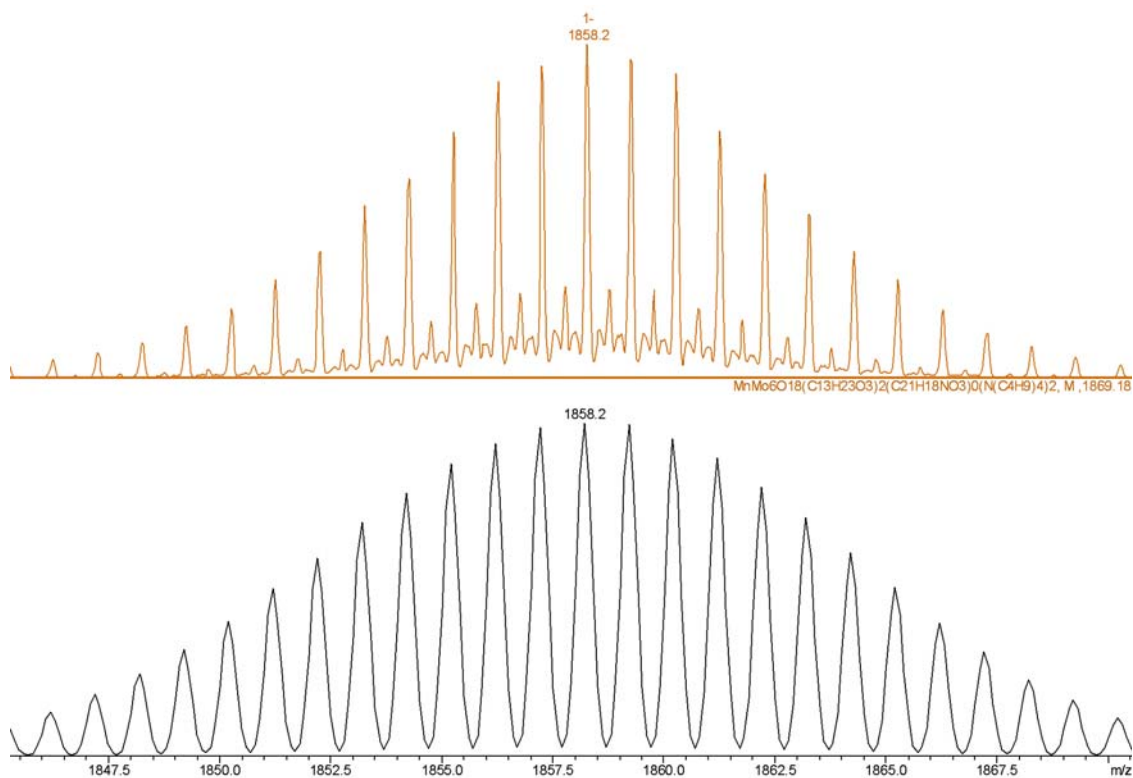


Figure S8: ESI-MS spectra of compound **2** shown in orange, with the simulated spectra underneath for comparison.

### Thermogravimetric Analysis:

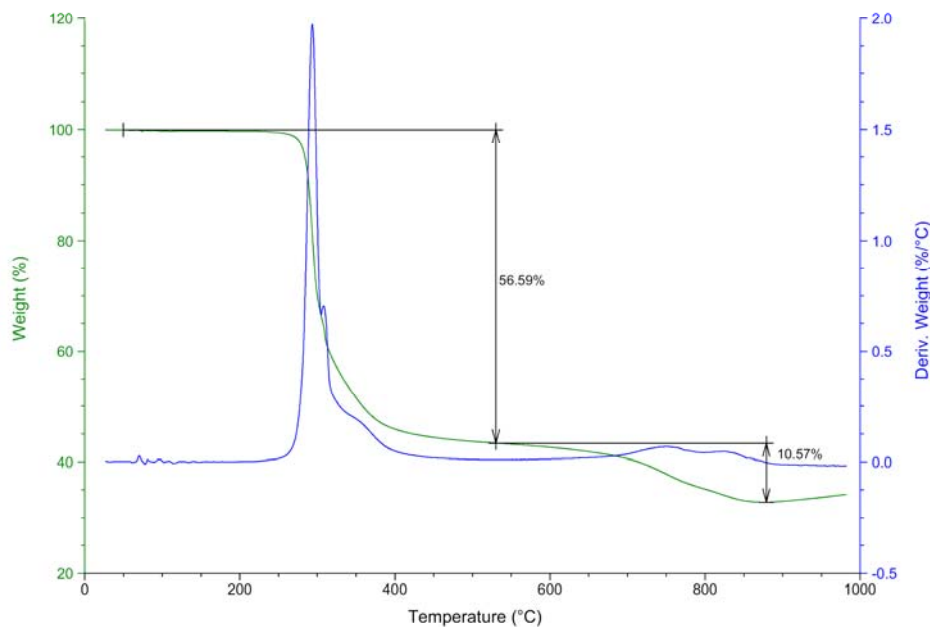


Figure S9: TGA analysis of compound **2**.

Thermogravimetric analysis of the material shows that it is stable up to 280 °C. It then starts decomposing from 280 °C to 530 °C, and there is a weight loss of 56.59 %, which correlates to the calculated loss of TBA cations and the alkene chains (56.3 %). This also corresponds to the phase change at 280 °C from the DSC data. There is a second weight loss of 10.67 % which is most probably due to a partial decomposition of the metal oxide. See figure S10.

### DSC Analysis:

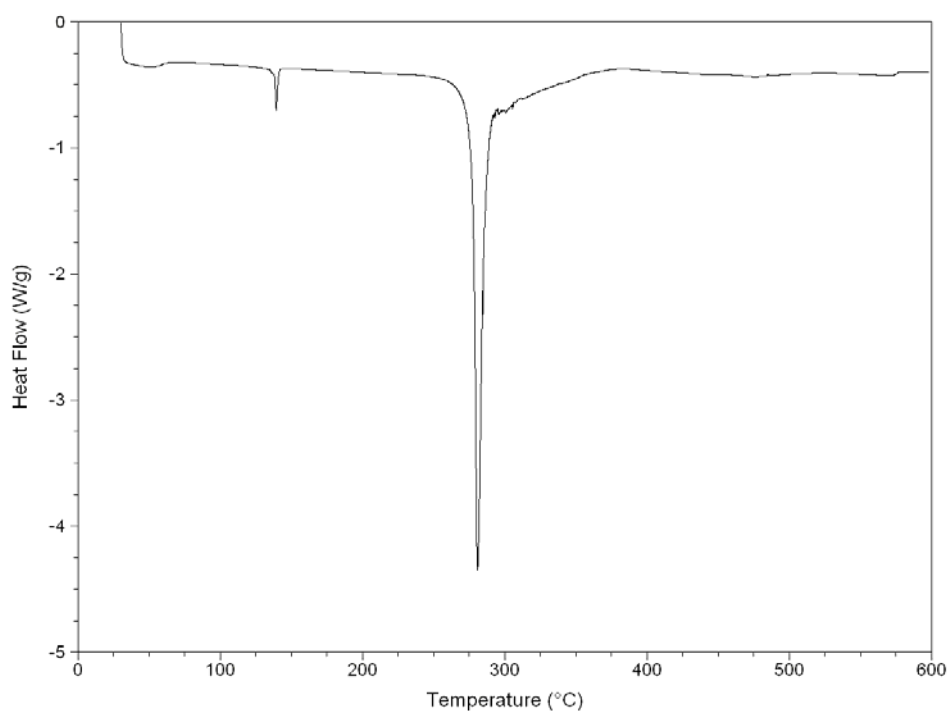


Figure S10: DSC analysis of compound **2**.

### Powder XRD analysis:

The Powder XRD pattern of the precipitate of compound **2** was collected, shown in orange, and compared to the simulated PXRD pattern from the single crystal X-ray, shown in black underneath, see figure S5. Neither display diffraction above  $50^\circ 2\theta$ , but well defined peaks are observed below  $15^\circ 2\theta$ . The PXRD pattern of compound **2** appears similar to that obtained from compound **1**, however it differs from the pattern obtained by simulation from the single crystal X-ray, possibly indicating that the precipitate forms in a different crystal structure to that of the single crystal.

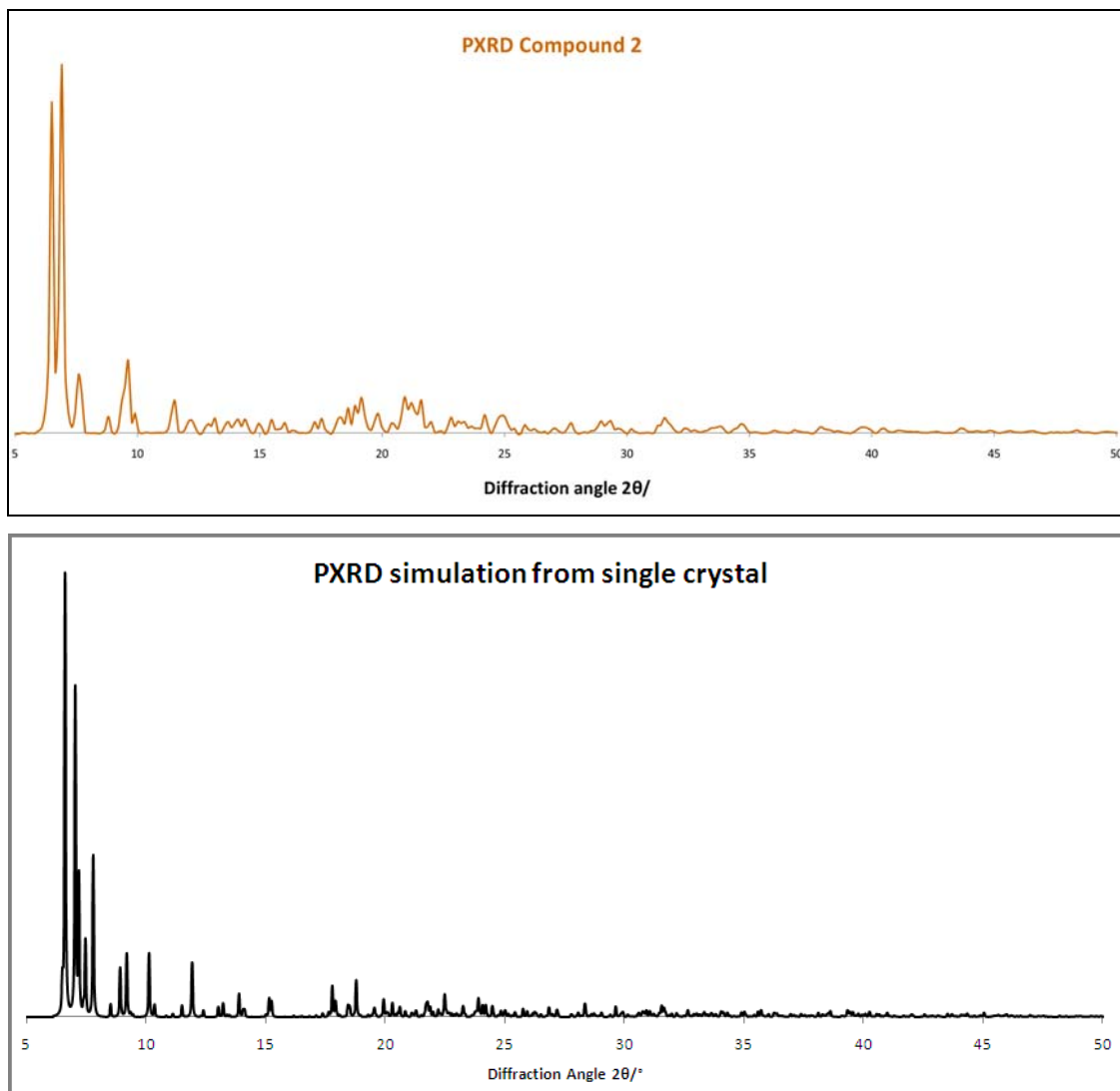


Figure 11: Powder x-ray diffraction of compound **2** (in orange), with the simulated powder x-ray pattern from the single crystal shown in black underneath.

### 3. *Synthesis and Characterisation of Compound 3*

From the same reaction pot as we synthesised compound **1**, we can also observe compound **3** from the fractional crystallisation by ESI-mass spectrometry. In order to synthesize sufficient material for full characterization and surface studies we used the method published in reference 2.

## Mass Spectra Discussion

Figure S12 shows the comparison of the different mass spectra obtained from the different compounds and compound mixes.

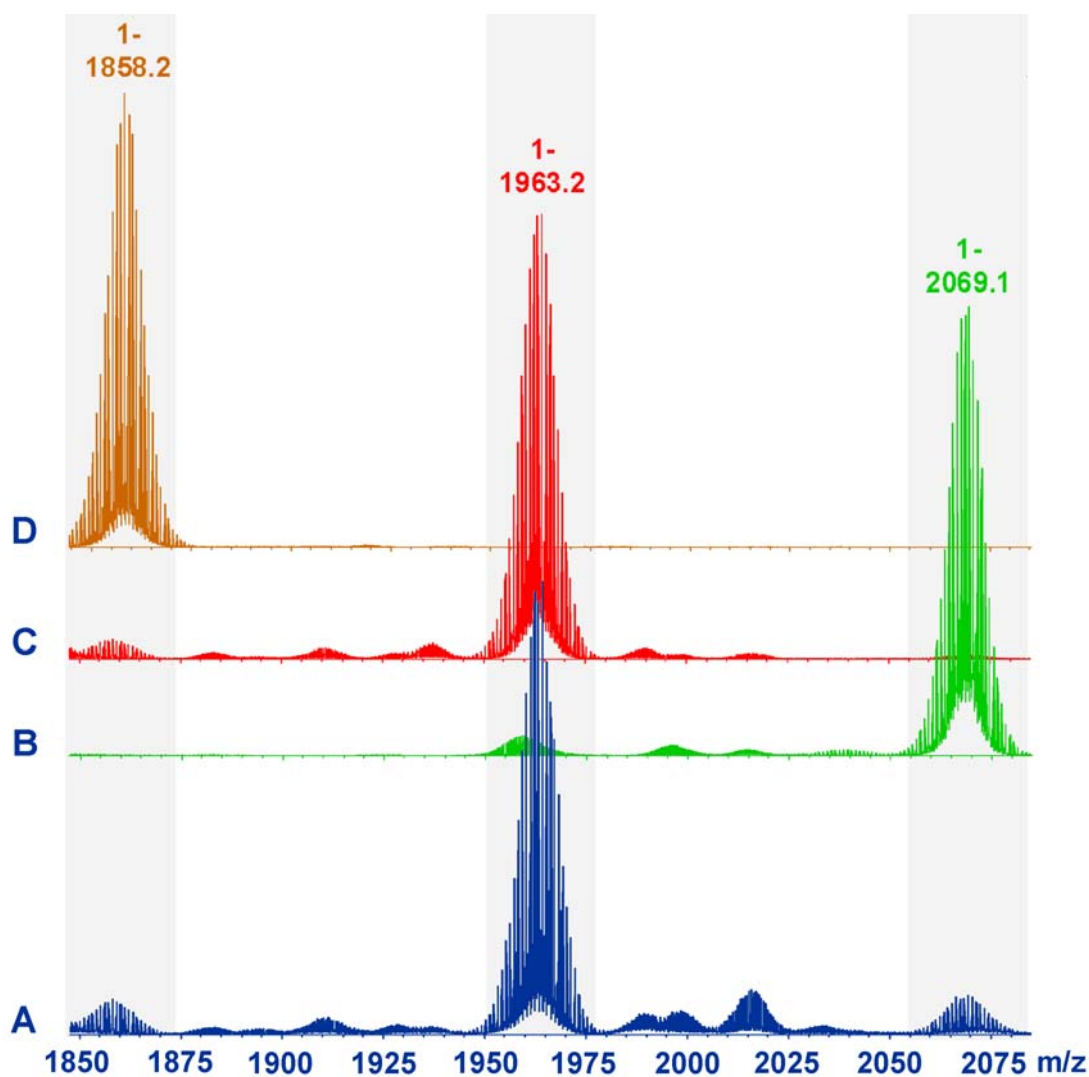


Figure S12: A is the mass spectra of the mother liquid before crystallisation, and shows a mixture of the three possible compounds, B shows the mass spectra of compound **3**, C shows the mass spectra of compound **1**, and D shows the mass spectra of compound **2**. The intensity ratio between the peak at 1963.2 to the peak at 1858.2 in A is 12:1, whilst in the purified spectra C, it is 22:1.

#### 4. UV Discussion

For an in depth discussion regarding the UV spectra of the sole Mn-Anderson, and for compound **3**, and how pyrene dominates the UV spectra see reference 2. The most important feature is the comparison of the  $\epsilon$  values of compound **3** and compound **1**. The  $\epsilon$  value of 1-pyrenecarboxaldehyde is  $13.2 \times 10^4$ , whilst the  $\epsilon$  value for compound **1** is  $20.9 \times 10^4$ , proving that there are two pyrene molecules present (all concentrations kept the same). The great interest in this context is that the  $\epsilon$  value for the compound **1** is  $11.6 \times 10^4$ , almost half the value of the **3**, and much closer the value for 1-pyrenecarboxaldehyde. This again proves that compound **1** is an asymmetric Mn-Anderson. It can also be seen that the  $\epsilon$  value for the compound **2** is  $7.2 \times 10^4$ , and as expected it is very similar to the symmetric TRIS Mn-Anderson at  $6.3 \times 10^4$ , hence the L2 present in compound **1** and **2** does not greatly affect the UV spectra.

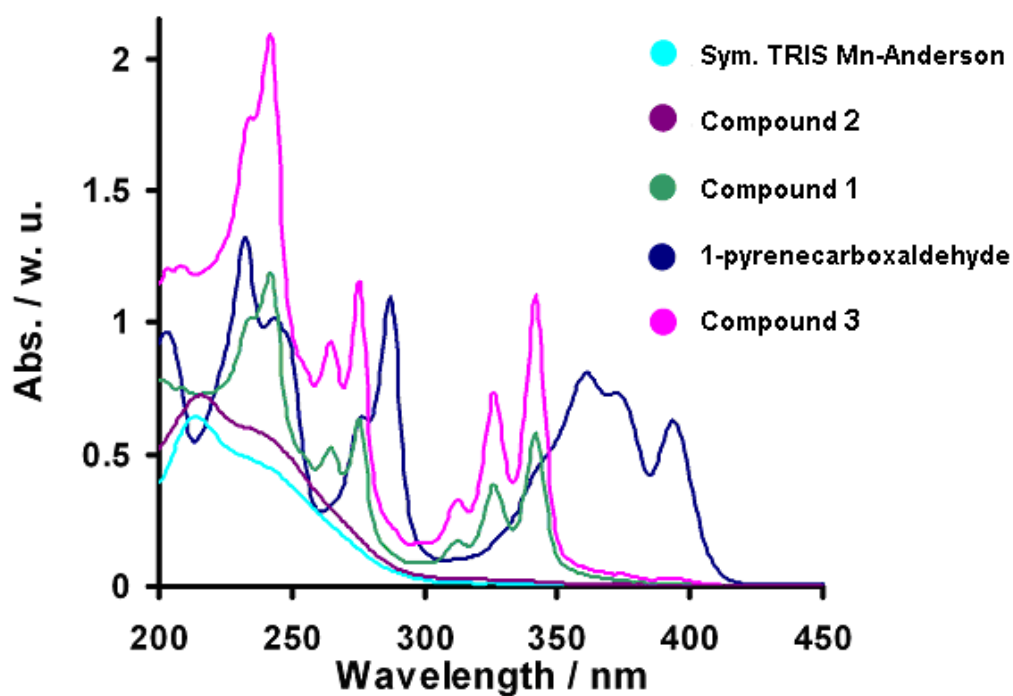


Figure S13: UV comparison for various Mn-Anderson compounds.



## 5. Self-assembly on surfaces

### *General Introduction:*

Self-assembly of compound **1-3** has been obtained at water/air interface by the Langmuir-Blodgett technique and film deposition has been carried out onto hydroxylated silicon substrates (SiOH). SiOH were obtained by treating native silicon oxide substrates through oxygen plasma (March Instrument Plasmod type Barrel, 1 mbar, 75 W, 10 min). SiOH substrates showed high hydrophilicity with a water contact angle of about 10° and a root mean square roughness (RMS) of about 0.2 nm has been observed by 1  $\mu\text{m}^2$  scanning force microscopy (SFM) images.

POM clusters were dissolved at a concentration of 0.5 mg/ml in a mixture of acetonitrile (Aldrich, 99.9%) and chloroform (Aldrich, 99.9%) with a volume ratio of 1:1. Drops (200  $\mu\text{l}$ ) of the above solutions were randomly spread over the aqueous subphase. After 20 min, the floating films were linearly compressed by two mobile barriers at a rate of 5 mm/min. Surface-pressure vs. molecular-area isotherms were recorded by film balance measurement. The monolayer at the air/water interface was stabilized for 5 min at the target pressure of 10 mN/m. Monolayer transfer was performed on SiOH strips about 2  $\text{cm}^2$  in size by an upstroke operation (vertical transfer) at speed of 5 mm/min. The LB layer deposited on SiOH was left to dry in air and successively observed by dynamic scanning force microscopy (SFM).

### *Investigation of Compound 1:*

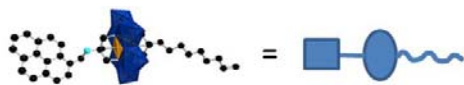
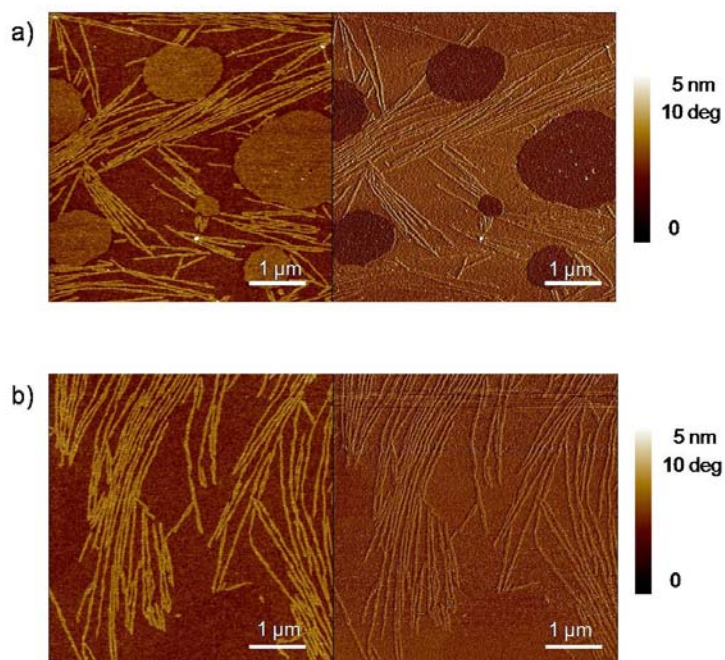


Figure S14: Schematic presentation of compound **1**.

The asymmetric Mn-Anderson self-assembles into nanoscopic fibers which typically laterally pair in ordered superstructures closely resembling biological fibrils. These fibrils are about 1-5  $\mu\text{m}$  long, and a cross section of average width of 60-70 nm and height of about 1 nm has been analysed, thus resulting in an aspect ratio (length:width) of 30:1.

Figure S15a shows a large scale topographic image where fibrils are clearly visible together with some circular islands (0.5-2  $\mu\text{m}$  wide) which produce an inverse contrast in the correspondent phase-lag image on the right. The presence of circular domains is typically observed by LB films as a result of the minimization of the energy needed to create a domain boundary between coexisting phases that is proportional to the domain perimeter.<sup>5,6</sup> Thus, in this figure the coexistence of fibrils structures, that are quite unusual for LB films, and more “ordinary” LB circular domains is observed. However, the circular domains are typically about 1 nm tall, that is in agreement with a picture in which the hybrid POMs are not vertically oriented at the substrate surface (the long molecular axis measures about 3 nm), as it typically occurs in close packed or solid-like phases of amphiphilic molecules. Interestingly, the circular patterns disappear when the sample is heated for 5 min at a temperature of 100  $^{\circ}\text{C}$ , while the fibrils lay stably at the surface (Figure S15b). No conversion of the circular domains into fibril structures has been observed, since the density of fibrils on the surface does not change upon the thermal treatment.



However, these patterns disappear when the sample is heated for 5 min at a temperature of 100 °C. (Figure S15b).

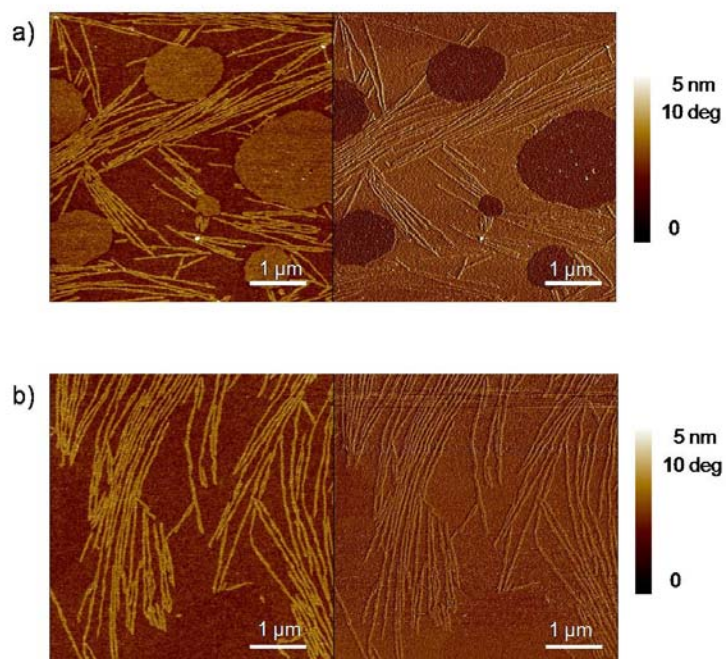


Figure S15: Topographic (left) and phase-lag (right) SFM images of compound **1** LB sub-monolayer transferred on SiOH before (a) and after (b) a thermal treatment at 100 °C for 5 min.

Thus the circular islands could be ascribed to an amorphous layer of hybrid POMs that desorbs with the thermal treatment likely because of the inclusion/solvation of water molecules.<sup>7</sup>

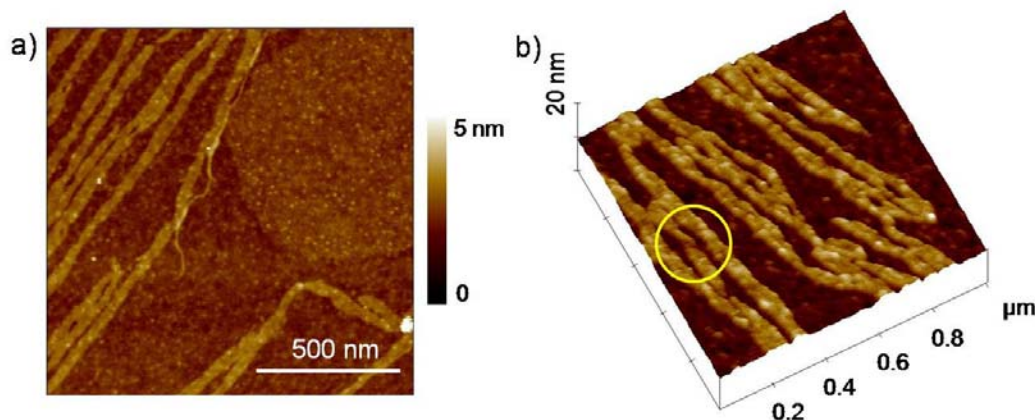


Figure S16: a) Restricted region of fig. 15a; b) 3D view of the LB nanostructures of compound **1**.

Figure S16 shows some more details on the fibres structure. In particular, the images highlight that there are different sizes of fibres, one that seems to be the most populated size, with a smaller sized fibre growing next to/out of the main fibre at certain points. They also seem to sometime join back up with the main fibre in some areas (figure S16a). Moreover, many crossing points are visible in which fibres seem to twist (see the marked circle in figure S16b as an example). In view of that, we can depict a typical fibril-like structure as formed by a number of paired fibres. On this respect figure S16 is very illustrative: different structural sizes are visible on the same region. Section analysis along the line marked in this image shows that the narrowest observed fibre typically measure almost 0.8 - 0.9 nm in height, corresponding to the diameter of an individual POM cluster core, and less than 20 nm in width. The fiber width as measured by SFM is overestimated because of the well-known tip-size broadening effect. The effect can be evaluated by considering previously proposed tip-surface convolution models.<sup>8</sup> Accordingly, by assuming the nominal SFM tip radius of about 20 nm, a tip

broadening of the same order is expected thus suggesting that the effective fibre lateral size is consistent with one or at most few clusters aligned to form a single fibre.

The lateral pairing of a number of these fibers lead to the formation of larger structures, showing widths of 60-70 nm. Heights values almost twice that of the thinnest fibers are observed in correspondence of fibers crossing points, which generates twisted and wrapped structures.

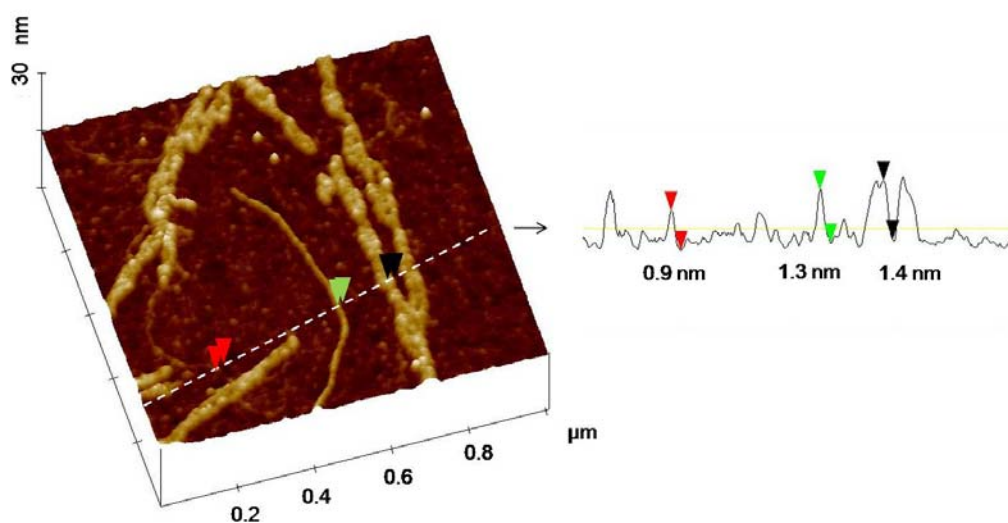


Figure S17: Restricted 3D view of compound **1** fibres of different sizes, and section analysis along the marked line.

A schematic picture of the suggested aggregation model is reported in figure S18, where the lateral pairing of the fibers to get fibril-like 2D superstructures is also depicted.

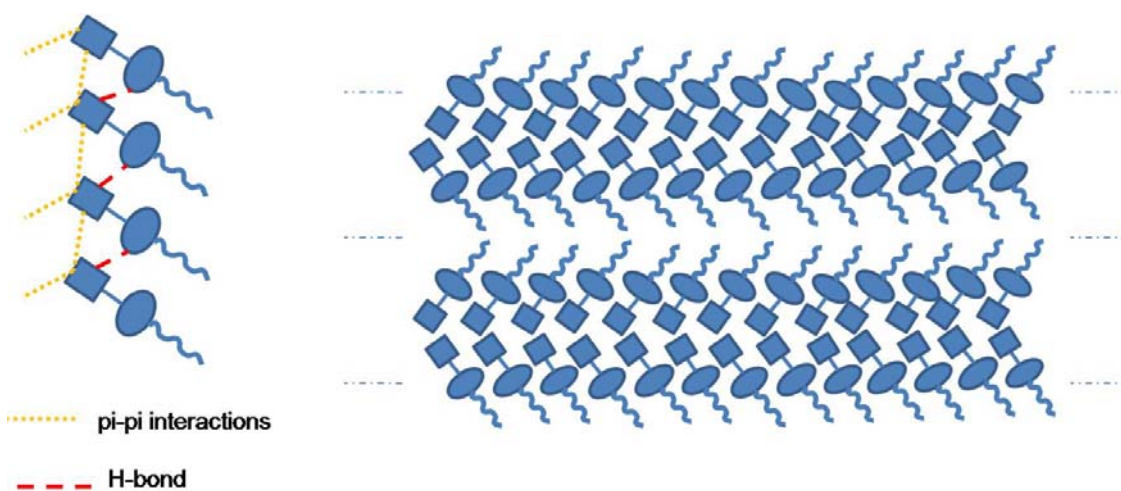


Figure S18: Schematic representation of the suggested molecular organization within the fibrils.



Accordingly, intermolecular bonds stabilizing the structure are both H-bonds between the cluster cores and the pyrene units ( $\text{C-H}\cdots\text{O}=\text{Mo}$ ), and  $\pi$ - $\pi$  interactions among the aromatic moieties.

### *Investigation of Compound 2:*

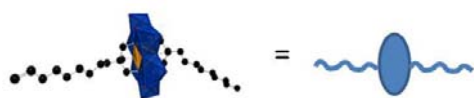


Figure S19: Schematic presentation of compound **2**.

Contrary to compound **1** and **3**, the symmetric C9 terminal alkene Mn-Anderson does not form fibres. This is shown in figure S20.

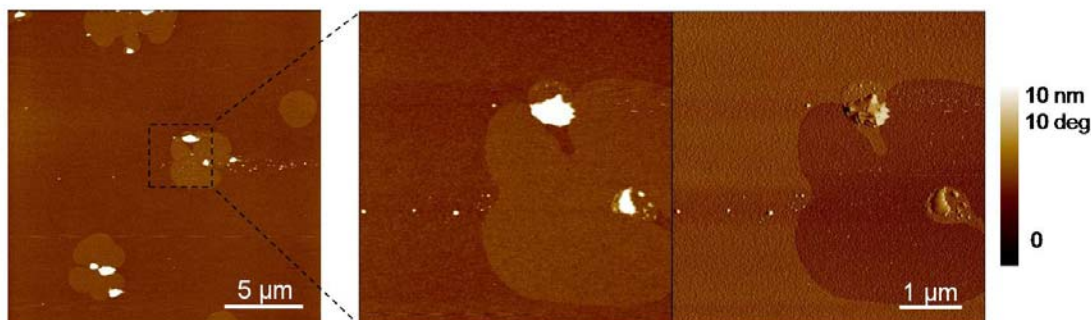


Figure S20: SFM images showing the LB pattern of compound **2** obtained on SiOH. On the right a close up topographic view is reported together with the corresponding phase-lag image.

At the same temperature and deposition pressure of **1** and **3**, compound **2** forms disconnected islands of 4-6  $\mu\text{m}$ . A thermal treatment at 100°C for 5 min produces the disappearing of the islands on the surface, as an indication that such a systems would likely consist of hybrid POMs including water molecules.<sup>7</sup>

In this case, differently of compound **1**, the barrier pressure doesn't allow for the formation of fibres (only random tall aggregates are visible besides the flat islands), thus indicating that the pyrene moiety has a determinant role in the fibres formation.

### Investigation of Compound 3:

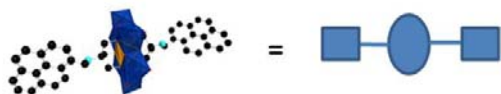


Figure S21: Schematic presentation of compound 3.

This symmetric pyrene-Mn-Anderson also shows a hierarchical organization into nanofibers and fibrils, but as a difference from compound **1**, the fibrils here are often not well aligned in the same direction. They have length of 0.2 - 1  $\mu\text{m}$ , along with average width and height of about 130 nm and 1 nm, respectively (see section profile in figure S22). Moreover, the aspect ratio of the anisotropic structures is in this case notably decreased down to 6:1, as a result of a relatively more important lateral pairing with respect to the fibres of compound **1**. The above effects agree with pyrene groups playing a decisive role in the lateral pairing of the fibers, as depicted in the model of figure S18, and also giving higher rigidity to the structure.

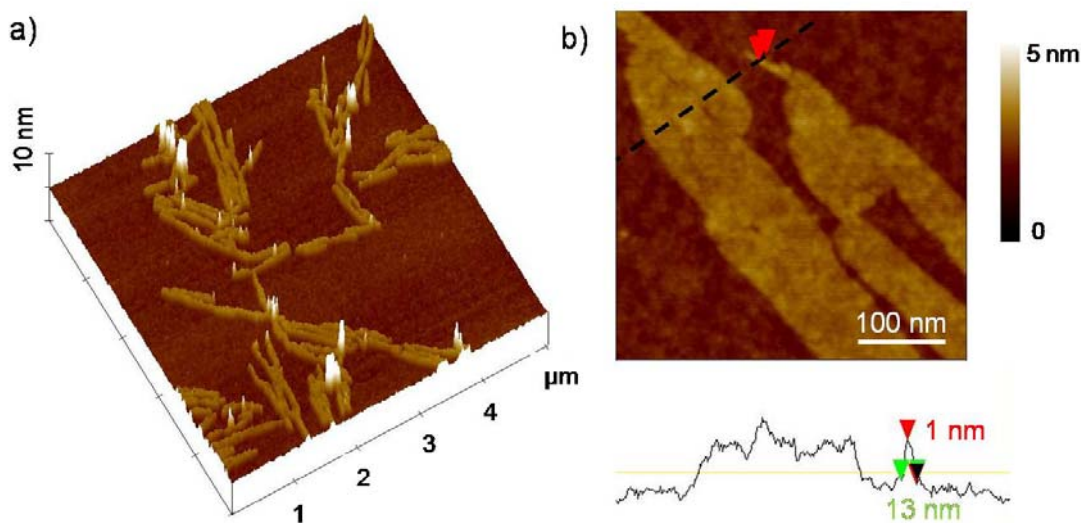


Figure S22: Anisotropic structures obtained by LB deposition on SiOH substrates. a) 3D large view b) zoom in a restricted region of a), with the section analysis along the marked line, highlighting height and width size of the smallest observed fibre.

As the model in figure S23 suggests, compound **3** can form structures that may be stabilized by a large number of  $\pi$ - $\pi$  and H-bond interactions, thus likely resulting in more rigid and paired structures, with respect to compound **1**.

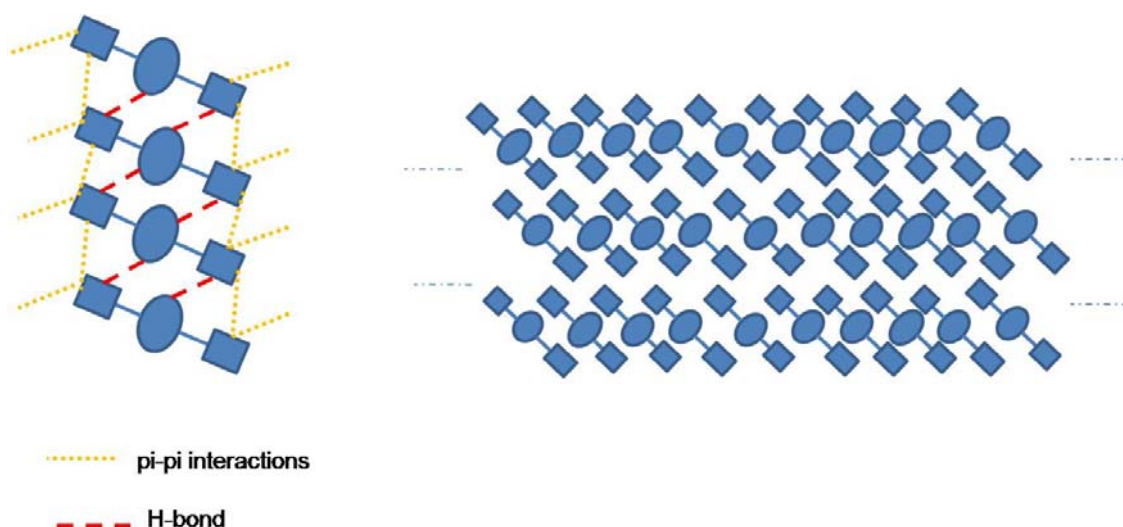


Figure S23: picture showing the possible arrangement of compound **3** within the fibre. The possible H-bond and pi-pi interactions among the pyrene groups are highlighted.

### *Comparison and Discussion of the three compounds on SiOH:*

In conclusion, we have demonstrated that hybrid POMs are suitable systems for the construction of anisotropic supramolecular and supermolecular architectures on surfaces.

In order to achieve such a result both chemistry and the deposition condition play a crucial role. In particular, the important role of the organic moieties is evidenced by the fact that the formation of long, narrow and regular fibrils is possible only when both one aromatic moiety and one alkene tail are grafted to the POM core. Shorter but larger and less aligned fibrils result by symmetric Mn-Anderson hybrids with two aromatic moieties, and no fibres have been observed for Mn-Anderson hybrids with two alkene tails. Thus, we can conclude that the pyrene moieties promote the extensive fibres lateral pairing through  $\pi$ - $\pi$  or C-H $\cdots$ O=Mo bonds (enthalpic factor), and that the lateral growth in asymmetric hybrids POMs, can be hampered by alkene tails, which in turn allow for a more pronounced growth in length. In addition to a weaker interaction by the aliphatic tails, the loss of lateral growth and the concomitant increase in fiber length might be at least in part ascribed to an entropic driven process dealing with the unfavourable ordering of long interacting organic tails.

As to the deposition conditions it has to be noted that, when these compounds are deposited by drop casting their solutions onto Si-OH, no 1D anisotropic features are



observed. Thus, the above peculiar self-structuring clearly arises by a pressure-induced molecular orientation at the air/water interface, condition that we forced by employing LB.

Also, no correlation have been found between the LB transfer direction and the fibers orientation at the solid substrate, so that their formation is expected to be not connected to the transfer process. This fact is corroborated by the evidence that such structures can be found also on other substrate like on mica. Finally SFM measurements on these structures after 6 months of aging showed no important alterations, indicating that the hierarchical organization induces quite high stability.

## 6. X-ray Crystallography

Suitable single crystals were selected and mounted onto the end of a thin glass fiber using Fomblin oil. X-ray diffraction intensity data were measured at 150(2) K on a Oxford Diffraction Gemini Ultra diffractometer using  $\text{Cu-K}\alpha$  radiation [ $\lambda = 1.54184 \text{ \AA}$ ]. Structure solution and refinement were carried out with SHELXS-97<sup>9</sup> and SHELXL-97<sup>9</sup> via WinGX.<sup>10</sup> Corrections for incident and diffracted beam absorption effects were applied using analytical methods.<sup>11</sup>

### 1. Crystallographic studies of $(\text{TBA})_3[\text{MnMo}_6\text{O}_{24}\text{C}_{34}\text{H}_{41}\text{N}]$ (1).

Crystal data and structure refinement for  $(\text{TBA})_3[\text{MnMo}_6\text{O}_{24}\text{C}_{34}\text{H}_{41}\text{N}]$  (1)  $M_r = 2205.63 \text{ g mol}^{-1}$ ; block shaped crystals;  $0.18 \times 0.13 \times 0.06 \text{ mm}^3$ ;  $T = 150(2) \text{ K}$ . Monoclinic, space group  $P2_1/c$ ,  $a = 24.6269(2)$ ,  $b = 14.3093(2)$ ,  $c = 26.7863(2) \text{ \AA}$ .  $\beta = 91.5980(10)^\circ$ .  $V = 9435.65(17) \text{ \AA}^3$ ,  $Z = 4$ ,  $\rho = 1.553 \text{ g cm}^{-3}$ ,  $\mu(\text{Cu-K}\alpha) = 7.955 \text{ mm}^{-1}$ ,  $F(000) = 4552.0$ , 35651 reflections measured of which 9576 are independent ( $R_{\text{int}} = 0.0294$ ), 746 refined parameters,  $R1 = 0.0766$  and  $wR2 = 0.2630$  (all data).

### 2. Crystallographic studies of $(\text{TBA})_3[\text{MnMo}_6\text{O}_{24}\text{C}_{26}\text{H}_{46}]$ (2).

Crystal data and structure refinement for  $(\text{TBA})_3[\text{MnMo}_6\text{O}_{24}\text{C}_{26}\text{H}_{46}(\text{CH}_3\text{CN})_2]$  (2)  $M_r = 2182.69 \text{ g mol}^{-1}$ ; block shaped crystals;  $0.19 \times 0.15 \times 0.14 \text{ mm}^3$ ;  $T = 150(2) \text{ K}$ . Monoclinic, space group  $P2_1/c$ ,  $a = 23.9788(3)$ ,  $b = 16.1403(3)$ ,  $c = 25.4293(3) \text{ \AA}$ .  $\beta = 99.830(2)^\circ$ .  $V = 9697.3(2) \text{ \AA}^3$ ,  $Z = 4$ ,  $\rho = 1.495 \text{ g cm}^{-3}$ ,  $\mu(\text{Cu-K}\alpha) = 7.733 \text{ mm}^{-1}$ ,  $F(000) = 4528$ , 70117 reflections measured of which 17289 are independent ( $R_{\text{int}} = 0.0503$ ), 940 refined parameters,  $R1 = 0.0539$  and  $wR2 = 0.1584$  (all data).

## 7. References

- (1) Ginsberg, E. A. P., *Inorg. Syn.*, **1990**, 27, 78-79.
- (2) Song, Y. F.; Long, D. L.; Cronin, L. *Angew. Chem. Int. Ed.*, **2007**, 46, 3900-3904.
- (3) Muth, A.; Asam, A.; Huttner, G.; Barth, A.; Zsolnai, L. *Chem. Ber.*, **1994**, 127, 305-311.
- (4) Pignataro, B.; Chi, L. F.; Gao, S.; Anczykowski, B.; Niemeyer, C. M.; Adler, M.; Blohm, D.; Fuchs, H. *Appl. Phys. A* **2002**, 74, 447-452.
- (5) Matsumoto, M.; Watanabe, S.; Tanaka, K.-i.; Kimura, H.; Kasahara, M.; Shibata, H.; Azumi, R.; Sakai, H.; Abe, M.; Kondo, Y.; Yoshino, N. *Adv. Mater.* **2007**, 19, 3668-3671.
- (6) McConnell, H. M. *Annu. Rev. Phys. Chem* **1991**, 42, 171-195.
- (7) Consalvo, C.; Panebianco, S.; Pignataro, B.; Compagnini, G.; Puglisi, O. *J. Phys. Chem. B* **1999**, 103, 4687-4692.
- (8) Garcia, V. J.; Martinez, L.; Briceno-Valero, J. M.; Schilling, C. H. *Probe Microsc.* **1997**, 1, 107-116.
- (9) Sheldrick, G. M. *Acta Crystallog. A*, **2008**, 64, 112-122.
- (10) Farrugia, L. J. *J. of Appl. Crystallogr.*, **1999**, 32, 837-838.
- (11) Clark, R. C.; Reid, J. S. *Acta Cryst. A*, **1995**, 51, 887-897.